28th AIAA Applied Aerodynamics Conference
28 June - 1 July 2010, Chicago, Illinois

AIAA 2010-4381

Design of a Swept-Wing Laminar Flow Control Flight Experiment for Transonic Aircraft

Michael J. Belisle,[1] Tyler P. Neale,[2] Helen L. Reed,[3] and William S. Saric[4]
Texas A&M University, College Station, Texas, 77843-3141

This paper addresses the conceptual design of a flight-test experiment incorporating a laminar flow control (LFC) wing glove on a business-jet-type aircraft. These experiments are designed to extend the spanwise periodic discrete roughness element (DRE) technology to chord Reynolds numbers between 15-20 million at a unit Reynolds number of 1.6 million per foot. A number of key questions were addressed and it is shown that: (1) it is possible to find an aircraft that can be used as a platform for this experiment and the selection converged on the Gulfstream II (G-II) based on suitability and expected availability; (2) a CFD of the aircraft flowfield showed that there is no interference from engines that would compromise the experiment. A computational grid for the G-II was created, and engine nacelle effects are "accountable" in the outboard section and the flowfield is spanwise-uniform where the glove would be located. Also, streamline deflections are accountable including AoA and in-plane deflection effects on the glove; and (3) it is possible to design an airfoil with a representative C_l and C_p distribution making DREs feasible. An airfoil section was designed that suggests NLF (natural laminar flow) is possible at AoA = 0°, with potential for DRE control between AoA = -0.5 and -1°.

I. Introduction

TEXAS A&M University has conducted a conceptual design study of a Laminar Flow Control (LFC) flight test with target conditions of Mach number M = 0.75 at an altitude H = 40 kft with a chord Reynolds number Re_c between 15 and 20 million, a unit Reynolds number Re' of 1.6 million per foot, and a leading-edge sweep angle Λ of 30°.

As background, Saric et al. (1998) discovered that transition delay is possible on a swept wing using a judiciously designed C_p distribution coupled with a passive spanwise-periodic discrete roughness element (DRE) distribution near the attachment line. The initial Saric experiments were conducted on a 45° swept wing in the ASU Unsteady Wind Tunnel at a nominal chord Reynolds number of 2.4 million and unit Reynolds number of 400,000 per foot. The Flight Research Laboratory at Texas A&M has completed a successful demonstration of the use of DREs to passively maintain a laminar boundary layer on a 30° swept wing at a chord Reynolds number of 8 million and unit Reynolds number of 1.6 million per foot (Saric, Carpenter, & Reed 2010; Rhodes, Reed, Saric, Carpenter, & Neale 2010) in flight. In addition, this promising technique has been demonstrated for supersonic flight (Saric, Reed, & Banks 2004).

Roughness receptivity studies are also presently underway under these conditions in order to quantify the role of roughness amplitude in generating crossflow waves (Carpenter, Saric, & Reed 2010). As a companion to this effort, Rizzetta, Visbal, Reed, & Saric (2010) have successfully applied accurate solutions of the disturbances generated by the micron-sized roughness as upstream conditions for the nonlinear parabolized stability equations.

The logical extension of these LFC efforts is to higher chord Reynolds numbers of 15–20 million under transport flight unit Reynolds numbers, and this is the topic of this abstract. Two issues exist related to the application of DREs in LFC. The first is unit Reynolds number, Re', which governs the roughness Reynolds number, Re_k. The proper sensitivity to roughness must be understood. The second is Re_c, which governs the overall stability behavior. It is well known that as Re_c increases, maintaining laminar flow becomes more difficult. Thus, the next step selected

[1] PhD Student, Department of Aerospace Engineering, Member AIAA
[2] Masters Student, US Air Force SMART Scholar, Department of Aerospace Engineering, Member AIAA
[3] Professor, Department of Aerospace Engineering, Fellow AIAA
[4] Distinguished Professor, Department of Aerospace Engineering, Fellow AIAA

Copyright © 2010 by the American Institute of Aeronautics and Astronautics, Inc. All rights reserved.

is to develop a workable, cost-effective, crossflow-dominated flight platform to raise the TRL of the DRE technology at unit Reynolds numbers characteristic of transports before going to full chord Reynolds numbers of 30 million.

Therefore, the question of feasibility of such an experiment involves three parts: (1) Is it possible to find an aircraft that can be used as a platform for this experiment? (2) Given the aircraft, does a CFD of the aircraft flowfield show that there is no interference from engines and control surfaces that would compromise the experiment? (3) Is it possible to design an airfoil with a representative C_L and C_p distribution that makes DREs feasible? The following tasks were conducted:

1) Aircraft Selection. An extensive list of aircraft were identified and examined for suitability as flight-test platforms. Candidates included a NASA Gulfstream II and Gulfstream III (G-II and G-III) and the Flight Test Associates (FTA) Sabreliner – 80 (S-80).
2) Aircraft CFD. A complete CFD analysis of the candidate aircraft was conducted following Rhodes et al (2010). The aircraft geometry was measured in detail, and both inviscid and viscous computations were performed. The influence of both the fuselage and the engine nacelles on the wing flowfield were of particular interest since the goal was to test under "spanwise uniform" conditions. Next a wing glove was designed within the newly modeled flowfield.
3) Airfoil Design. A laminar flow, swept airfoil was designed to operate at conditions of Mach number M = 0.75 at an altitude of H = 40,000 ft thereby achieving transport-flight unit Reynolds numbers (1.6 million per foot). The chord Reynolds numbers are in the range of Re_c = 15–20 million and the C_L is 737-like. The target leading-edge sweep angle is Λ = 30°. Passive and DRE techniques were considered. Both linear stability theory (LST) and nonlinear parabolized stability equations (NPSE) were applied to determine the feasibility of DRE techniques in maintaining laminar flow.

II. Aircraft Selection

A wide range of aircraft were surveyed to determine which optimized several different criteria for the program. The first major requirement was to select an aircraft which could achieve the desired 15-20 million Re_c. Primary factors influencing Re_c include wing chord length, cruise speed, and cruise altitude. Coupled with the targeted 30° wing sweep and the eventual extension to transport aircraft, a business-jet platform presented a suitable class of aircraft for this phase of the research.

Over 70 different business jets were initially examined as potential candidates for the project. To gather information about each of the aircraft, the online database *Jane's Aircraft Upgrades* (Jane's 2009) was utilized. Once the list of candidate aircraft was completed, each aircraft was given a pass-fail grade according to the following criteria: fuselage-mounted engine nacelles, a cruise speed of Mach 0.8, a cruise altitude of 40,000 ft., and a wing sweep angle of 30 degrees. Any aircraft that did not satisfy all four of these basic criteria was eliminated from the candidate list, significantly reducing the number of potential aircraft.

After this first reduction, chord lengths were examined on the remaining candidate aircraft (to meet chord Reynolds number), again further reducing the number of candidate aircraft for the project. Finally, the availability of extant aircraft for the flight test was examined. The project would require an estimated six months for the flight test and exclusive use of the selected aircraft during this testing time frame. Removing and reapplying the wing glove and instrumentation could prove difficult and affect the results. Permission would also be needed to modify the aircraft by mounting a wing glove and installing necessary equipment. Therefore, aircraft owned by flight testing organizations remained the only ones suitable, and those available through leasing agencies were eliminated.

Considering all of the criteria and requirements previously stated, the final candidate aircraft consisted of the G-II, the G-III, and the S-80. These three similar aircraft met all of the performance specifications and had fuselage-mounted engines. The G-II and G-III were available through NASA-DFRC and the S-80 was available through FTA. Both agencies would allow modification and extended, sole-use flight testing. Table 1 lists various specifications for the three selected aircraft.

Table 1. Downselected aircraft specifications.

Aircraft	Wing Span (ft.)	Wing Sweep (c/4)	Max Cruise Speed (Mach)	Max Altitude (ft.)
S-80	44.5	28.5°	0.8	45,000
G-II	68.83	25°	0.85	43,000
G-III	77.83	27.67°	0.85	45,000

Through discussions with NASA-DFRC and FTA during the initial stages of the project, the selection of the aircraft converged on the NASA G-II/SP with tail number N949NA (shown in Figure 1 below). Since the G-II is larger than the S-80, the desired chord Reynolds number would be more easily obtained. While the G-III had a larger chord still, it was unavailable during the planned six-month flight test time period.

With this selection, the next step was to perform a full CFD analysis of the aircraft. While the results from the CFD tests would be specific to the G-II, any conclusions reached could be qualitatively extended to the G-III and S-80 in case plans for the test-bed aircraft changed. In fact, since the G-III uses the same power plant as the G-II, results from the G-II study could be considered very applicable to the G-III. Also, upon further consideration, the team decided to design the experiment to a cruise Mach number of 0.75 (rather than 0.8) so as to avoid supercritical conditions on the wing glove given the thickness-to-chord constraints. This decision affected neither the top 3 candidate aircraft selections nor the objectives of the experiment.

Figure 1. The NASA G-II/SP (N949NA) on a tarmac in El Paso, TX.

III. Feasibility of the NASA G-II/SP

With the selection of the G-II for flight testing, a full CFD study of the flowfield was conducted to determine any effects the fuselage, control surfaces, and engine nacelles may have on the wing flowfield. With the nacelles impinging slightly over the G-II wing near the root, the availability of regions of "spanwise-uniform" flow to apply the wing glove had to be confirmed.

A. Laser Scanning

The first step in the CFD process is obtaining a CAD model of the aircraft of interest. Often times, these models are available through the manufacturer. However, there can be proprietary reasons for manufacturers not being able to release this information, and the CAD models of older aircraft are sometimes inaccurate. When models are not available, a viable solution is performing a laser scan of the aircraft and creating a CAD model from the data.

Since a readily-available model of the G-II was not available, Direct Dimensions, Inc. (DDI) from Owen Mills, MD was contracted to perform a detailed laser scan of the aircraft and subsequently create a three-dimensional CAD model. This model would, in turn, be implemented into a CFD solver to calculate the aircraft flowfield. Scanning occurred over two days at the NASA Forward Operating Location in El Paso, TX, where this particular G-II was residing.

To scan the aircraft, DDI used a Surphaser 25 HSX medium-range laser scanner, which delivered single-point accuracies of about 0.01 in. The G-II was placed on jacks for the duration of the scan and was housed inside a hangar. To reduce both scanning time and cost and computational time in creating the model, only half of the aircraft was scanned, treating a vertical plane through the center of the aircraft as a plane of symmetry. The empennage of the G-II was also ignored during the scanning process since it would have no effect on the wing flowfield (Rhodes et al. 2010).

With the scanned data of the G-II, DDI then developed a solid CAD model of the aircraft. Since one of the primary goals of the CFD study was to determine the effects of the engine on the wing's flowfield, multiple variations of the G-II model were created. The first contained a "flow-through nacelle" that had no faces at the inlet or outlet of the engine, allowing the air to flow freely through the nacelle. While this model would capture the aerodynamic effects of the nacelle inlet, it would not be able to simulate any effects of the turbofan. It also would not represent an accurate flow rate through the nacelle. The second model, called the "closed nacelle" model, contained solid faces at the inlet and outlet of the engine, preventing any flow from passing through. These faces could later be assigned boundary conditions in order to simulate the effects of an operating engine. The final model

variation did not contain any of the nacelle structure on the aircraft. This "no-nacelle" model was created to serve as a baseline so that results obtained with this model could be compared to the models containing the nacelle. This would allow conclusions to be made regarding the influence of the engine on the flowfield. Views of the generic CAD model are seen in Figures 2 and 3.

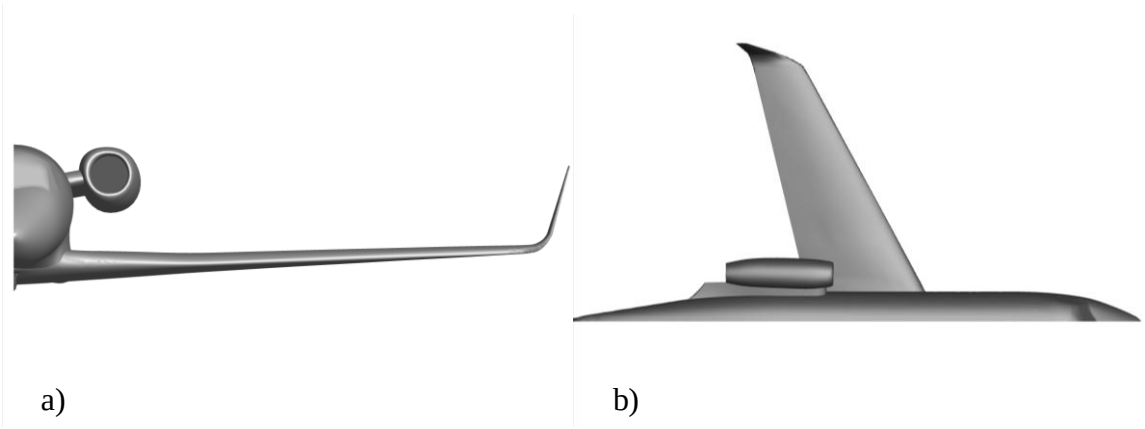

Figure 2. CAD model created from laser scan: a) front view b) top view.

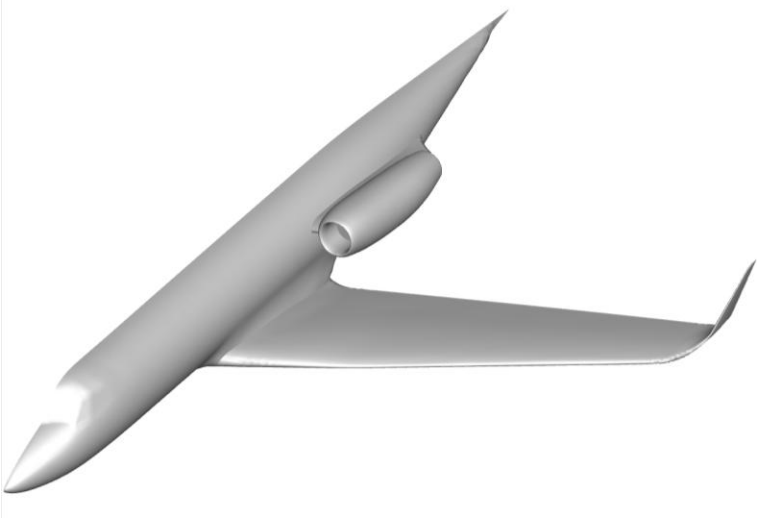

Figure 3. Isometric view of G-II/SP CAD model.

B. Grid Generation

Previous experiences with aircraft CFD studies provided a roadmap for the G-II. Extensive CFD work had been performed on a full aircraft model of the O-2 operated by Texas A&M's Flight Research Laboratory. Many techniques and lessons learned were discovered through this work, which were then extended to the G-II project. A flowfield domain was created around the scanned geometry provided by DDI (Rhodes et al. 2010) and the meshing program GAMBIT 2.3.16 (ANSYS Inc. 2010) was used for creating the computational mesh.

So that only half of the G-II aircraft was used for the CFD study, a vertical face cutting through the center of the fuselage was created to serve as the plane of symmetry, and symmetric flow was assumed on the port and starboard sides of the aircraft. As anticipated, the meshing process for the G-II model required numerous iterations. Building upon the technique developed for the O-2 study, a hybrid mesh consisting of several different volume mesh zones was created for the G-II. The zones consisted of a freestream volume, an aircraft volume, and a wing volume, shown in Figure 4. This setup permitted high-fidelity meshes in regions of interest without having needless detail in less important regions.

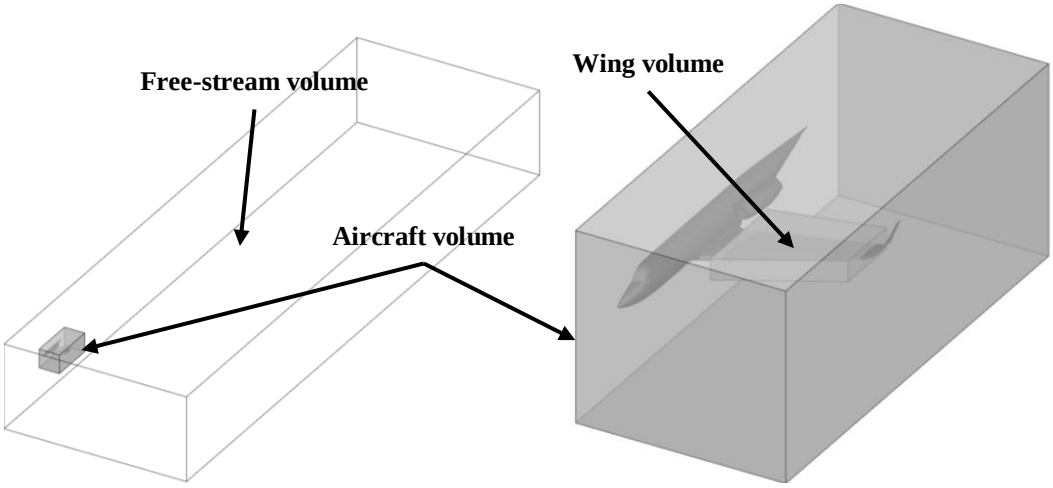

Figure 4. Overview of hybrid mesh setup.

The wing volume zone contained most of the aircraft wing. Since details of the pressure field on the wing were a key factor in this study, a high-fidelity mesh was preferred near the surface. A structured mesh around the wing would be able to achieve this required level of detail without incurring an unnecessarily high cell count. Higher cell concentrations were placed at the leading and trailing edges and near the surface to allow the flow to be adequately resolved. Figure 5 shows the structured wing volume mesh created for the G-II.

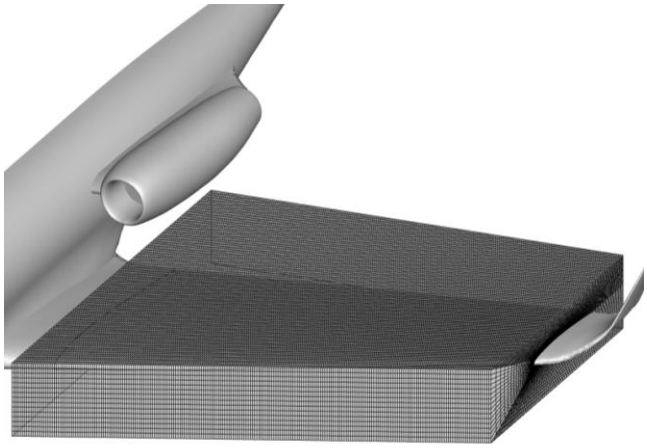

Figure 5. View of the wing mesh zone.

The next zone was the aircraft volume. The G-II model contained several complex geometrical features, necessitating an unstructured mesh since creating a structured mesh for such complicated geometry would be nearly impossible. All remaining parts of the aircraft not contained in the wing volume zone had a tetrahedral surface mesh. Since the aircraft surface was present in the structured wing zone and the unstructured aircraft zone, its surface mesh contained both types of elements. Much care needed to be taken during this meshing process, as the likelihood of highly skewed elements increased due to the complexity of a tetrahedral mesh. Avoiding this required both user experience and multiple iterations of the meshing process starting with the edge meshes. The aircraft volume mesh can be seen in Figure 6.a.

Since minute details of the flow were not needed in regions far from the aircraft, a structured volume mesh was again used for the freestream zone. This allowed the far-field details of the flow to be modeled without causing a high cell count. This structured mesh was tailored so that as the distance from the unstructured volume mesh around

the aircraft increased, the cell sizes increased as well. The dimensions of the freestream zone needed to be such that any boundary effects would not affect the solution. Placing any boundary too close to the aircraft geometry could skew the flowfield results. The freestream mesh can be seen in Figure 6.b.

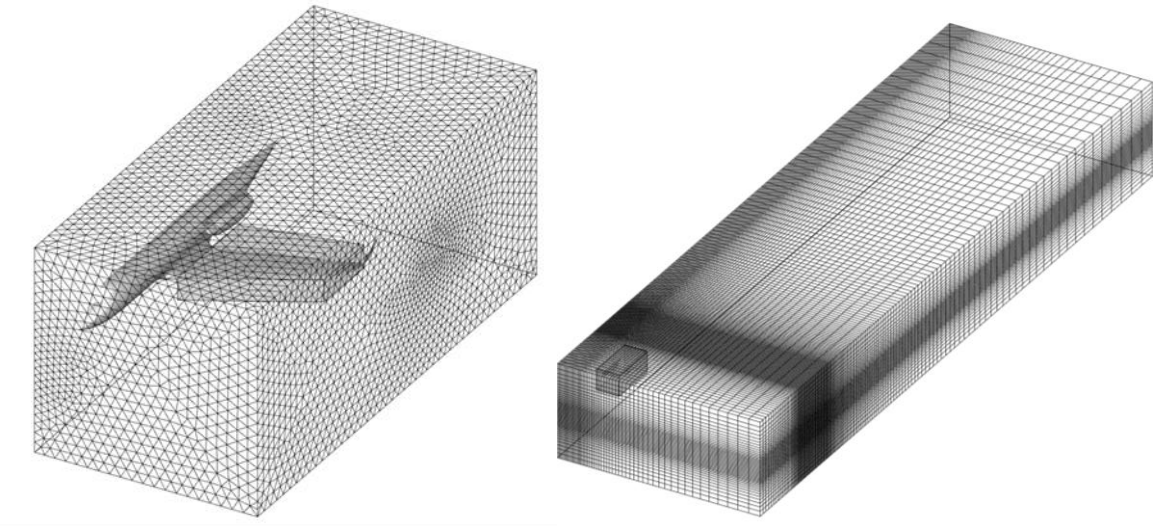

a) b)

Figure 6. Views of the outer mesh zones. a) Aircraft mesh zone. b) Freestream mesh zone.

The final computational mesh consisted of over 4.5 million cells, with the majority coming from the unstructured aircraft mesh. While this was a significant amount of cells, it was still less than the number of cells in the O-2 mesh. The use of structured elements for the freestream volume dramatically reduced the cell count in the mesh. Table 2 shows the different cell counts for each mesh zone. The entire domain extended 750 ft. in the streamwise direction, with the aircraft residing in roughly the front quarter of the span. The spanwise dimension of domain extended about 120 ft. from the centerline of the aircraft. The domain extended about 100 ft. both below and above the aircraft.

Table 2. Cell counts for the different mesh zones.

Zone	Cell Count
Wing Mesh (Structured)	911,250
Aircraft Mesh (Unstructured)	3,176,254
Free-stream Mesh (Structured)	420,600
TOTAL	**4,508,104**

To demonstrate grid independence, two more grids were created in a similar manner as the baseline grid discussed above. One consisted of very fine elements around the wing and aircraft, while the other grid used coarser elements in these regions. For completeness, a fourth grid was developed that extended the flowfield domain in all three axes. Results generated from all grids could then be compared during post-processing to ensure they matched.

C. Flowfield Calculations

The CFD studies were performed using the commercial FLUENT 12.0.16 (ANSYS Inc. 2010) CFD software package. A viscous, pressure-based solver was used, and compressibility effects were included. Initial targets for the flight test were a speed of Mach 0.75 at 40,000 ft. The atmospheric values at this altitude, as specified by US Standard Atmosphere 1976, are a freestream static pressure of 393 psfa (18.8kPa abs) and static temperature of 390 °R (217 K). The air was treated as an ideal gas to determine air density and the angle of attack of the aircraft was 0°.

1. Engine modeling

Properly modeling the G-II's engines provided an added challenge to the flowfield calculations. Boppe (1984) explained the spillage and blockage associated with the engine's inlet can propagate on to an aircraft's wing. This could affect the G-II since its nacelles are positioned near the root and partially over the wing. Since flowfield disturbances on the wing caused by the engine could dramatically affect the wing-glove placement, it was vital to the experiment to determine the extent of any engine effects. This would be accomplished using the three variations of the G-II model previously mentioned.

The closed model required specific conditions at the inlet and outlet, leading to the development of a modeling methodology. As explained in Flack (2005), the first component of a turbofan engine is the diffuser, or inlet. The primary purposes of the diffuser are to deliver a smooth and uniform flow of air into the compressor and to decrease the air velocity to a speed suitable for the compressor. Mattingly (2006) explains that an engine compressor typically operates best with a flow in the range of Mach 0.5. As a divergent channel, the diffuser uses its aerodynamic properties to accomplish the reduction in flow velocity to the on-design condition of about Mach 0.5, thus increasing the static pressure of the flow. This increase in static pressure caused by the diffuser represented a primary area of interest for the project, as this could affect the pressure distribution across the G-II wing. It was important to be able to model both the aerodynamic effects of the engine inlet as well as the fan face. By placing the boundary condition on a plane near the location of the engine's fan face, the flow would be able to naturally develop in the diffuser before reaching the boundary. With this in mind, an appropriate boundary condition at the fan face inside the engine was needed to model the effects of the engine. It was determined that the most appropriate method for modeling the effects of the engine involved specifying a target mass flow rate at the fan face. With this boundary condition, FLUENT would adjust the static pressure value at the boundary for each iteration until it achieves the target mass flow rate. Based on the explanation in Mattingly (2006), the specified mass flow rate at the fan face should eventually bring the flow velocity to about Mach 0.5 under ideal, on-design conditions. To utilize this boundary condition, an appropriate mass flow rate was needed for the G-II engine. Seddon & Goldsmith (1999) explain that during cruise conditions, aircraft engines typically operate in a "spillage" mode, which indicates the nacelle does not accept the entire flow at the inlet. This leads to a typical mass flow ratio (MFR) between 0.8 and 0.5 for the engine inlet (Mund, Doulgeris, & Pilidis 2007). The MFR is defined as simply the ratio between the mass flow actually accepted and the ideal mass flow based on engine inlet area and no flow blockage. Based on the area of the engine inlet, the ideal mass flow rate would be about 30 kg/s for flight conditions of Mach 0.75 at 40,000 ft. This is termed the "reference" condition in Table 3.

For initial calculations, simple CFD cases consisting of only the G-II engine were created. Significant time was saved by first modeling only the engine and then applying the lessons learned to the full-aircraft model. Operating conditions were again specified at Mach 0.75 at 40,000 ft. First, the flow-through nacelle solution was used to examine the aerodynamic effect on the pressure field caused only by the engine's inlet. After obtaining a converged solution, the mass flow rate passing through the engine of the flow-through nacelle model was found to be roughly 24 kg/s. Even without a boundary at the fan face, about 20% of the flow was still being blocked, indicating that the closed nacelle cases should have lower mass flow rates than the flow-through nacelle case since the effects of the fan face will also be included.

Next, mass flow rates were specified at the fan-face boundary of the closed nacelle model. MFR values of 0.8, 0.6, and 0.5 based on the unobstructed mass flow rate of 30 kg/s were used for the simulations. The MFR of 0.5, equating to only 15 kg/s, represented the worst-case scenario, as it allowed the least amount of flow to enter the engine. Anything worse than this case should not be encountered during cruise conditions. However, having such an extreme condition can help bracket the effects of the engine on the wing. The results from the three closed nacelle cases and the flow-through nacelle case were then examined to determine the effects of different MFR values on the static pressure near the engine.

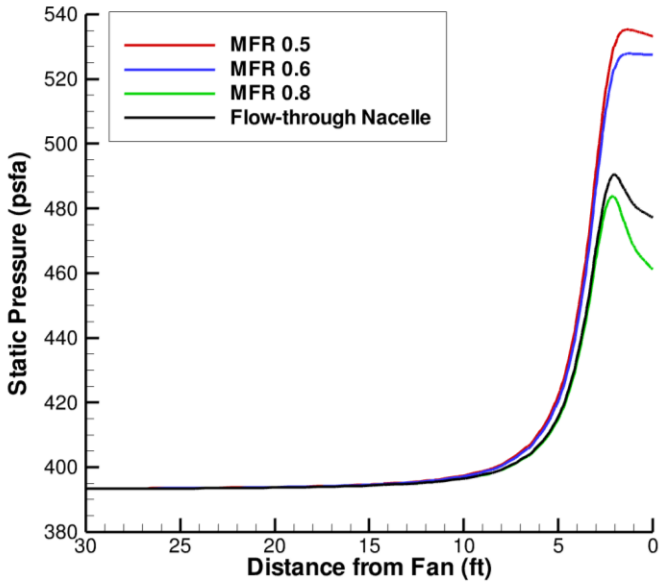

Figure 7. Static pressure plots of the four engine models.

As seen above in Figure 7, all four cases exhibited similar behavior near the fan face. The pressure values were taken along a line that passed through the center of the nacelle and travelled far upstream. The flow-through case and the 0.8 MFR case caused the lowest pressure increases since they accepted the highest mass flow rates. The pressure increase can also be seen to propagate upstream, indicating that it could have an effect on the pressure distribution of the wing.

To confirm the validity of the different MFR values used, the Mach number of the flow at the fan face was also examined. As previously mentioned, compressors typically operate best with incoming flow at about Mach 0.5. Therefore, it was assumed that during standard cruise conditions, the flow should ideally enter the compressor of the G-II engine in this Mach range. The results of the CFD cases showing the fan face Mach numbers can be found in Figure 8. From the plot, an MFR of about 0.73 should result in the ideal, on-design fan face velocity of Mach 0.5. The range of MFR values used for this study was shown to be reasonable for simulating the effects of the engine on the flowfield. The results also allowed a better understanding of how the different specifications at the fan face boundary affected the solution.

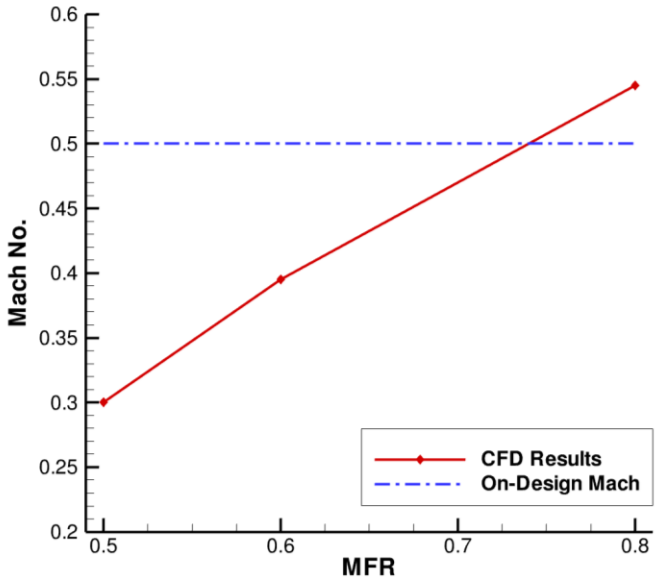

Figure 8. Fan face Mach numbers at different MFR values.

With the inlet boundary condition determined, the engine exhaust was then examined for the closed-nacelle model. Specifying the mass flow rate at the outlet served as the most appropriate boundary condition. The exhaust of the G-II engine is a convergent nozzle, and the flow exiting should be at a sonic condition. Therefore, ideally, the flow at the exhaust should be at Mach 1.0 in a converged CFD solution. Parameters that would primarily affect the Mach number of the flow at this boundary condition were the mass flow rate and the total temperature. This exhaust mass flow rate was specified for all closed nacelle cases, regardless of the mass flow rate specified at the inlet. While this did not technically obey mass conservation for the engine, it allowed the sonic condition at the exhaust to be maintained. Preserving mass continuity through the engine would not affect the solution. Also, the cases with low mass flow rates would not necessarily be realistic during flight, as they are simply worst-case scenarios used to determine the effects of a pressure rise at the inlet. Therefore, maintaining the sonic condition at the exhaust by keeping the mass flow rate fixed at 24 kg/s was considered the most appropriate technique for the engine model.

2. Results

Once the proper solver settings and boundary conditions were determined, solutions were obtained for the different full-aircraft CFD cases. Table 3 details the mass flow rates used for these cases based on the results from the closed nacelle CFD cases. The primary focus for the results was the pressure distribution on the wing. By comparing solutions of the no-nacelle model to different cases of the closed nacelle model, the effects of the engine could be determined. A relatively spanwise-constant pressure distribution is of importance as a suitable location for the wing glove. Interference from the engine could introduce atypical flow patterns on the wing, thus adversely affecting the wing glove flowfield.

Table 3. Inlet mass flow rates specified for each model. A 0.73 MFR corresponds to an ideal fan-face Mach number of 0.5. An exhaust mass flow rate of 24 kg/s corresponds to sonic conditions at the exhaust.

Model	Inlet Mass Flow (kg/s)	Exhaust Mass Flow (kg/s)
Reference	*30*	*30*
0.8 MFR	24	24
0.73 MFR	22	24
0.6 MFR	18	24
0.5 MFR	15	24

To view the effects of the engine on the wing pressure field, Figures 9 and 10 show C_p plots at 25% and 45% semi-span, respectively. Here, semi-span is measured with respect to the aircraft centerline, and only accounts for usable wing span, that is, the winglet was not included in the total span since the wing glove could not be mounted in this location. The 25% semi-span plot is almost directly below the engine, thus causing the dramatic difference between the three MFR cases and the no-nacelle model. A much more adverse pressure gradient is present on the MFR cases, progressively worsening as the mass flow decreases. However, at 45% semi-span the effects are much less noticeable. While the pressure gradient is still shallower, it closely resembles that of the no-nacelle model. These results indicate that further outboard, the pressure field may be suitable for the wing glove. While these plots show a local view of the engine effects, a more global view of the pressure distribution on the wing is necessary to draw more concrete conclusions.

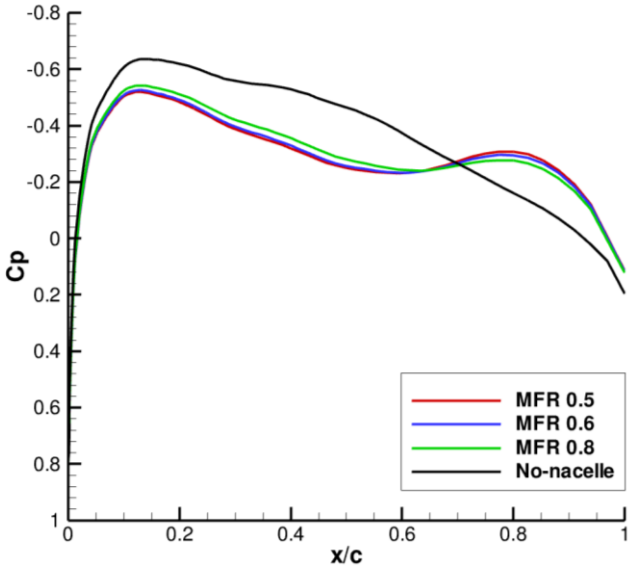

Figure 9. C_p data at 25% semi-span.

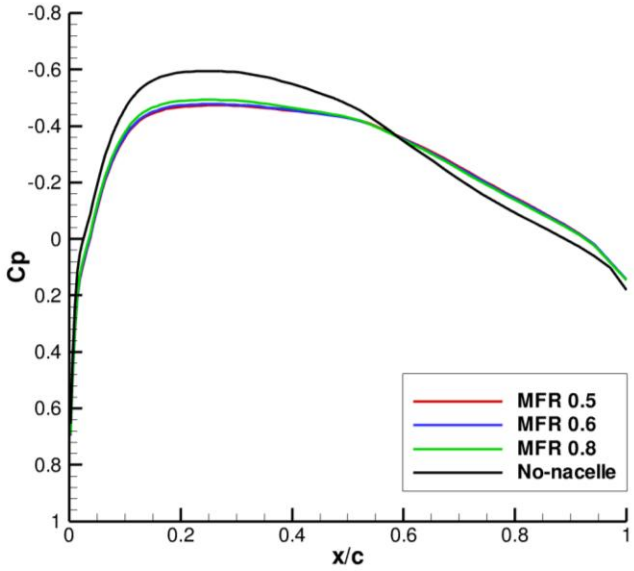

Figure 10. C_p data at 45% semi-span.

Presented first in Figure 11 are the pressure contours for the no-nacelle model. The wing is delineated by increments of 10% semi-span. The pressure distribution is relatively spanwise constant. Next, the results from the 0.8 MFR case are presented in Figure 12. As anticipated, the static pressure increase at the engine inlet propagated upstream and onto the wing. However, the effects are seen to dissipate further outboard on the wing.

Figures 13 and 14 show the more severe closed nacelle cases. Again, an adverse pressure gradient is present in the immediate region by the engine inlet for these two cases, with the effects dissipating further outboard. Since the 0.6 and 0.5 MFR cases have a lower mass flow rate and, thus, a higher pressure increase than the 0.8 MFR case, the effects by the engine are more severe. Of note is the increase of the high-pressure region directly below the nacelle as the MFR is decreased. However, the high-pressure region mostly vanishes near the 40% span mark for all MFR cases.

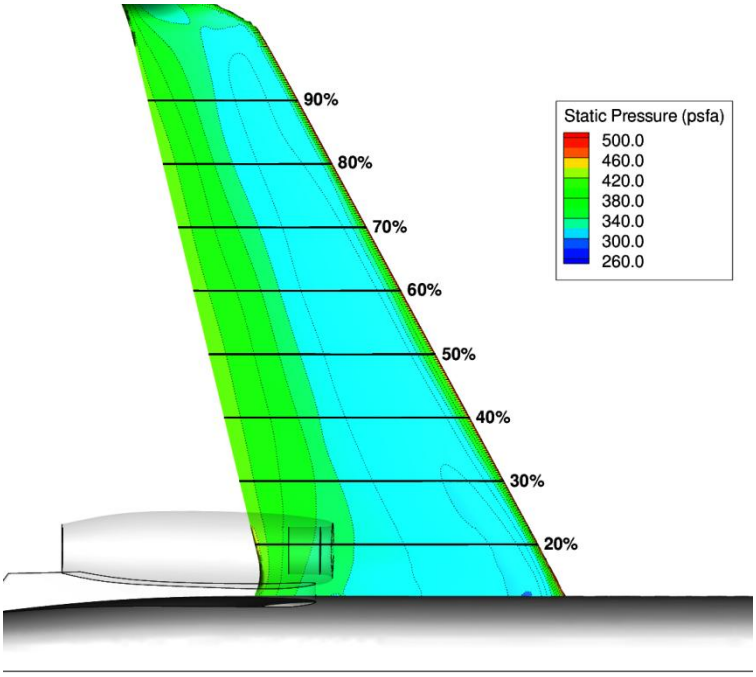

Figure 11. Pressure contours for no-nacelle model.

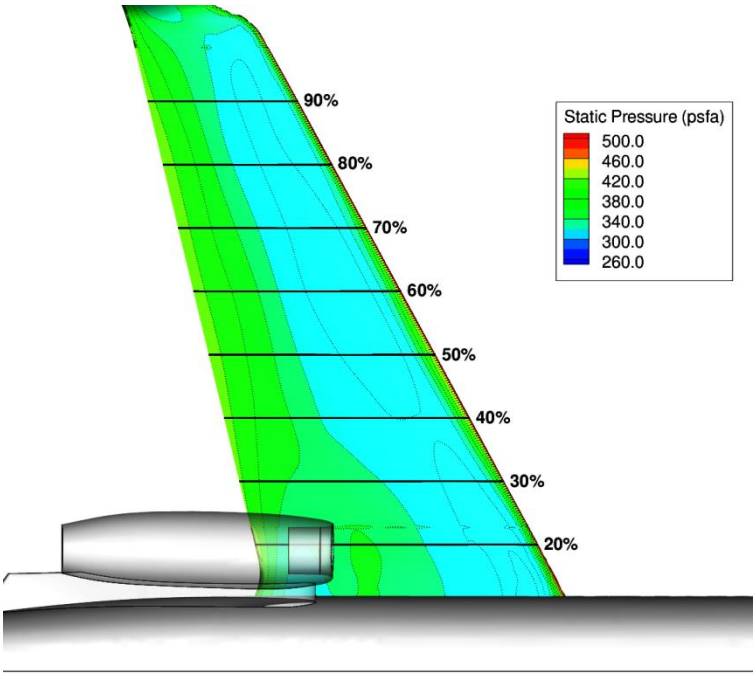

Figure 12. Pressure contours for 0.8 MFR closed nacelle model.

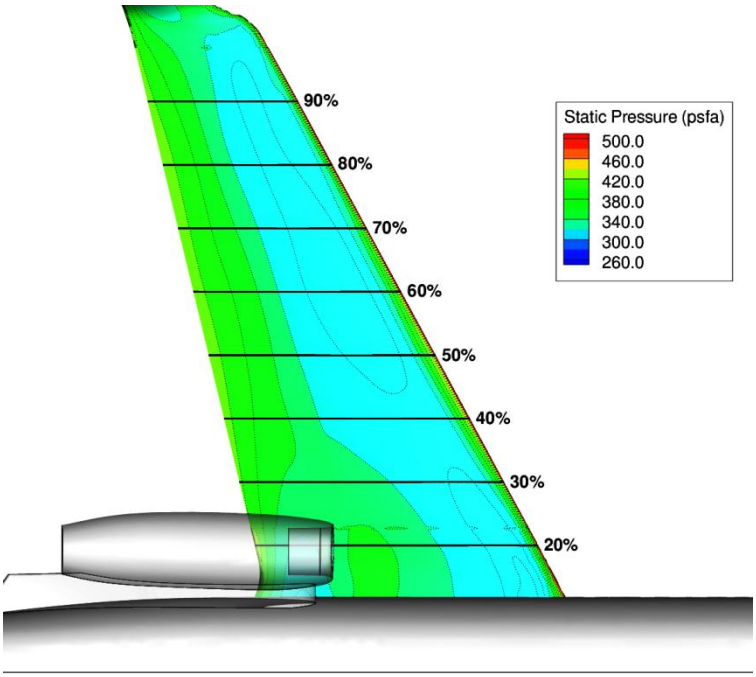

Figure 13. Pressure contours for 0.6 MFR closed nacelle model.

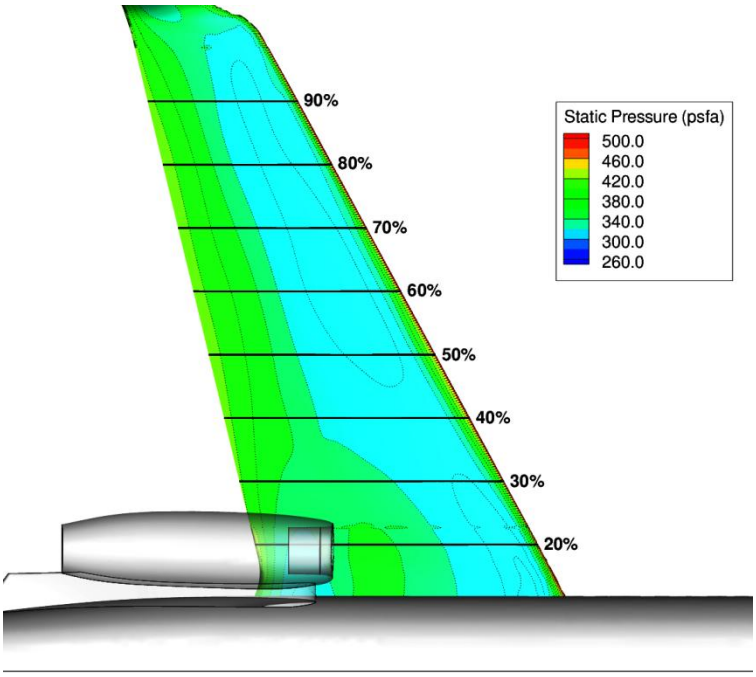

Figure 14. Pressure contours for 0.5 MFR closed nacelle model.

Despite the marked influence of the engine on the inboard section of the wing, the pressure effects dissipate at about the same rate for all three closed nacelle cases. These results indicate that outboard of about 45% semi-span, the pressure distribution on the wing can be expected to be relatively spanwise-constant, regardless of the mass flow rate of the engine. A close-up view of the pressure contours of the 0.5 MFR case showing the nearly spanwise-constant distribution is shown in Figure 15. The red region represents the suitable mounting area for the glove, while the dotted blue lines show the spanwise-constant pressure contours. Since this is the worst-case model, any location outboard of 45% semi-span should be suitable for the wing glove LFC experiment.

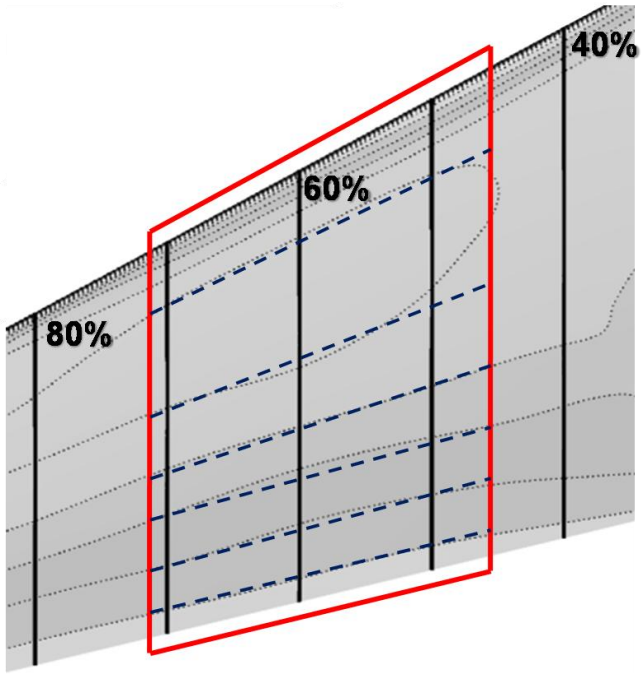

Figure 15. View of spanwise-constant pressure lines on MFR 0.5 case.

Next, the streamline deflection due to the fuselage was examined. Following the work of Rhodes et al. (2010), care must be exercised in relating experimental "freestream" measurements to true far upstream conditions because of limitations of the probe placement. For determining the streamline deflection, the tip of the air data probe for the wing glove on the G-II was assumed to be six inches below the glove's pressure side and two feet upstream of the leading edge. With a six-foot wing glove mounted on the aircraft at about 45% semi-span, the probe was assumed to be positioned at about 53% semi-span. Velocity component "measurements" (from the CFD) were taken along a horizontal straight line spanning from far upstream to the estimated probe tip location. Figure 16 shows the evolution of the apparent angle of attack (AoA) as the flow approaches the probe tip. The location of the aircraft nose is represented by the dashed blue line, and the wing root location is shown by the green dashed line. A small deflection in AoA (as seen by the air data probe) is predicted. However, a greater streamline deflection is experienced in the plane of the wing (IPSD; in-plane streamline deflection), as seen in Figure 17. Roughly speaking, the wing glove should experience about a 3 degree increase in apparent sweep due to the deflection. The glove will be designed in the context of the full-aircraft simulations so that both effects will be accounted for in the stability analyses.

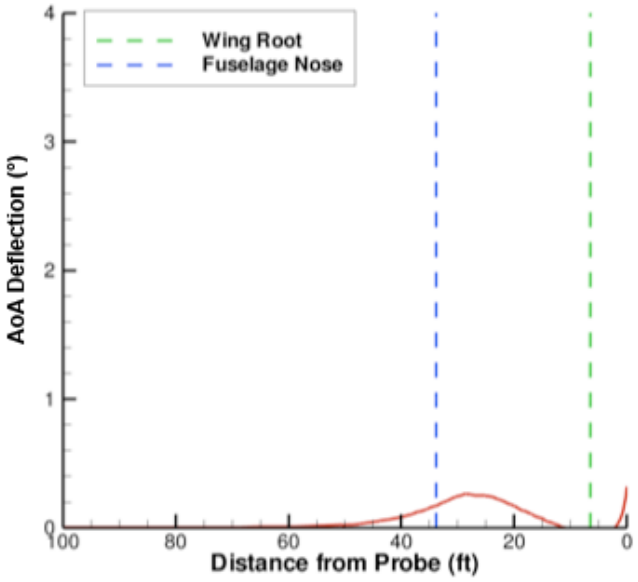

Figure 16. Variations in apparent AoA (from far upstream to the tip of the air data probe) due to streamline deflection.

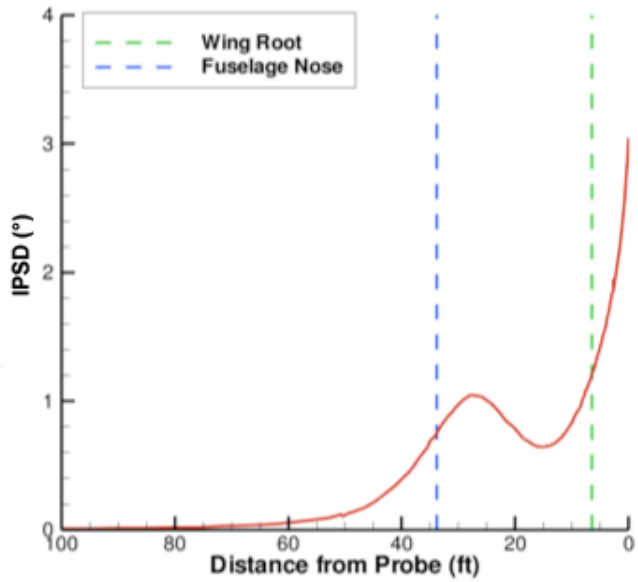

Figure 17. Variations in streamline deflection in the plane of the wing IPSD (from far upstream to the tip of the air data probe) due to streamline deflection.

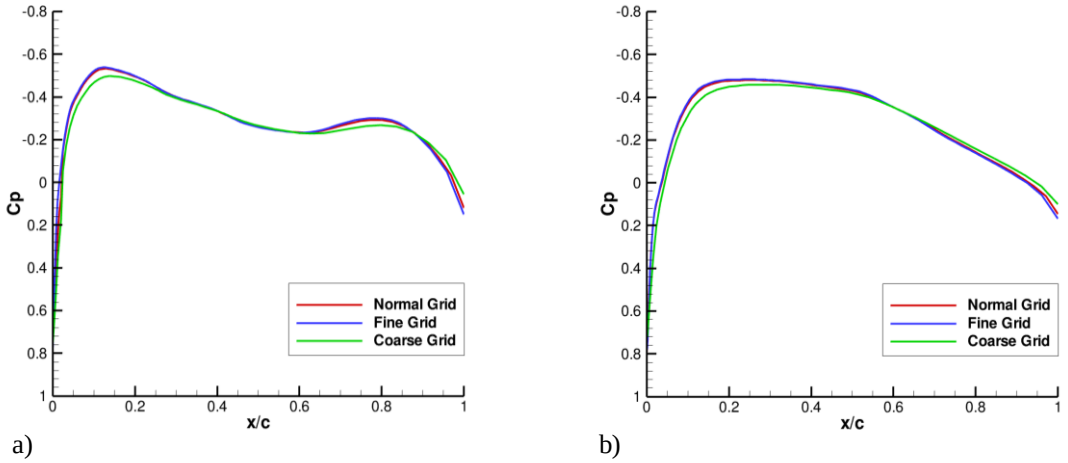

Figure 18. C_p comparison of three different fidelity grids. Semi-span: a) 25% b) 45%.

3. Verification

Verification of results is an important aspect of any CFD simulation. The first test checked for grid independence and utilized the varying fidelity grids discussed earlier. All results presented thus far were generated from the normal (baseline) grid (Table 2). Studies under the same conditions were conducted using the fine and coarse grids. As seen in Figure 18, all three grid have similar C_p values at two different wing stations. These results indicate that the normal grid was appropriately refined to capture the important physics of the flowfield.

The fourth grid was used to determine if the boundaries of the computational domain affect the flowfield solution. The interior meshes around the aircraft and wing remained the same as the ones used in the normal mesh version of the closed-nacelle model. A solution was obtained at the same operating conditions as the original model, and C_p values along the wing were compared as shown in Figure 19. The results are nearly identical, indicating the normal grid sufficiently models the flow without any effects from the boundaries.

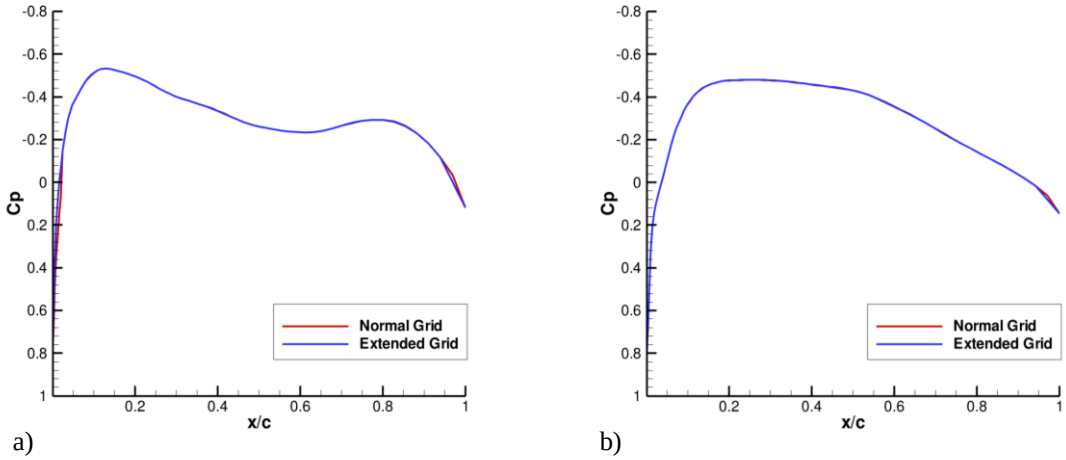

Figure 19. C_p comparisons of the normal and extended grids. Semi-span: a) 25% b) 45%.

D. Wing Glove

The most suitable configuration for the LFC flight tests is an instrumented wing glove, shown notionally in Figure 20 below. The glove extends to at least 60% of the experimental airfoil chord, truncating and recovering the pressure before the G-II/SP control surfaces are reached. Moreover the glove will be allowed to extend forward of

the aircraft wing (by no more than a foot) in order to meet t/c constraints while satisfying stability requirements for crossflow control. To generate the basic state for the stability analyses, a detailed full-aircraft Navier-Stokes CFD study will be conducted with the wing glove installed and including flow through the engines. This will allow the effects of the aircraft on the wing glove flow field to be accounted for in a manner similar to Rhodes et al. (2010). Moreover, fairings between the glove and the G-II/SP wing (in the spanwise direction and not shown in Figure) will be designed so as to ensure continuity of geometry, slope, and curvature, and eliminate those as possible receptivity sources for disturbances. The next section describes the process for generating the OML (outer mold line) for the glove.

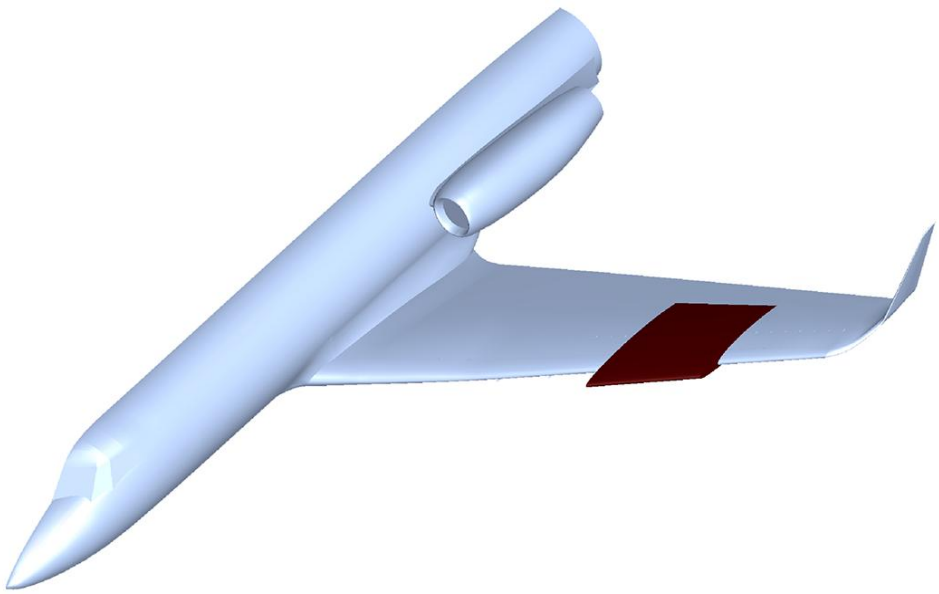

Figure 20. Notional wing glove on port side of G-II/SP. Note that fairings between the glove and wing in the spanwise direction are necessary and not shown here.

IV. Laminar Flow Control Airfoil

We have completed the preliminary design of a laminar flow airfoil section at M=0.75 to serve as the first iteration for the OML for the G-II wing glove, with the goal of laminar flow back to 60% chord on the suction side and, optionally, 50% chord on the pressure side. Note that the purpose of this study was to show the feasibility of and the methodology for designing the flight test experiment, and, with additional iteration based on results from the full-aircraft CFD including the glove (as described above) and nonlinear stability computations, the airfoil shape would be further optimized to meet DRE control objectives. This detailed refinement effort, however, has been put on hold as we were tasked to begin the development of a new airfoil OML and glove for the forthcoming experiment which is now to be flown on a different platform, a G-III, as will be explained in Section V.

Keeping in mind that the present work was a proof-of-concept and non-optimized study, the preliminary airfoil identified and designated as TAMU-003T-75, achieves the target C_L>0.3 for Re_c in the range of 15-20 million, avoids supercritical conditions, and meets thickness-to-chord (t/c) requirements for mounting on the G-II/SP wing. While the objective was to design an airfoil section such that laminar flow could be maintained through DREs, we found the added benefit that at off angles of attack, natural laminar flow (NLF; favorable pressure gradient) was effective in delaying transition.

The design philosophy conducive to DRE control is as follows. The main idea is to carefully design the pressure coefficient distribution and airfoil section so as to encourage crossflow, eliminate streamwise and attachment-line instabilities, and allow shorter wavelengths to grow sufficiently and early enough for control of the most unstable wavelength.

- An accelerated flow back to nominally 60% chord (on the suction side) will be (nearly) subcritical to streamwise instabilities (Tollmien-Schlichting waves; T-S). When considering natural or passive LFC on swept wings, it is unwise to work at the margins of this instability.

- To implement DRE control, it is recognized that in the low-turbulence flight environment, stationary crossflow is the dominant instability and surface roughness provides the initial condition for the instability. One first identifies the most unstable (or "critical") stationary crossflow wavelength, $\lambda_{critical}$ (it is easiest to reference this length as being parallel to the leading edge). Linear stability theory accurately predicts this critical wavelength and the location at which it first becomes unstable (neutral point).
- The favorable pressure distribution is then shaped so as to encourage shorter-wavelength stationary crossflow disturbances to grow earlier than the critical wave, but then decay downstream. The goal is for some of these shorter-wavelength disturbances to grow sufficiently in the leading-edge region to nonlinearly modify the mean flow and inhibit the growth of the critical disturbance. Thus transition will be delayed if one of these so-called "control" modes is made to dominate in the early-growth region through the application of roughness near the leading edge at these spanwise wavelengths.
- Limiting the normal-to-the-leading-edge radius r so as to satisfy the condition

$$\mathrm{Re}_{\theta AL} = 0.404[\mathrm{Re}' r \tan\Lambda \sin\Lambda / (1+e)]^{1/2} \le 100$$

  is necessary to eliminate the possibility of leading-edge contamination. Here $Re_{\bullet AL}$ is the attachment-line Reynolds number, Re' is the dimensional unit Reynolds number based on freestream conditions, Λ is the leading-edge sweep angle, and e is the leading-edge ellipticity. See Pfenninger (1965, 1977) and the VKI 2009 Course Notes "Advances in Laminar-Turbulent Transition Modelling".

The airfoil was designed using a workflow that included iteration on the geometrical design using XFOIL (Drela & Youngren 2001), flowfield calculations for an inviscid infinite swept wing using GAMBIT and FLUENT (ANSYS 2010), boundary layer calculations using WINGBL2 (Pruett 1994), and linear stability calculations using LASTRAC (Chang 2003). The parameters of the designed airfoil are shown in Table 4.

Table 4. Design parameters for TAMU-003T-75 airfoil.

	TAMU-003T-75
Mach number	0.75
Q_∞ (freestream speed)	221 m/s
t/c	9.3%
r	28 mm
Re_c	$17.2 \bullet 10^6$
$Re_\bullet$	86
C_L (AoA = 0°)	0.37

Linear stability calculations were iterated many times with airfoil calculations to shape the C_p distribution to minimize T-S instabilities while permitting controllable growth of crossflow. The measure of the stability behavior is the natural log of the amplitude ratio or the so-called N-factor. The resulting Euler C_p calculations are shown in Figure 21.

As seen in Figure 21, the lift coefficient of the designed airfoil ranges from C_L = 0.25 at AoA= -1° to C_L = 0.49 at AoA = +1°. The thickness ratio of t/c = 9.3% is feasible for mounting on the G-II/SP wing. As confirmed in the next paragraph with the companion stability results, the C_p distribution at AoA = 0° is characteristic of an NLF (without DRE control) airfoil for a swept wing, with a typically steep initial favorable pressure gradient near the leading edge on the suction side, followed by an accelerated region back to approximately 62% chord that excites stationary crossflow and limits the growth of T-S instabilities. The intent for an NLF airfoil is to balance these two instabilities without allowing either one to grow sufficiently to trigger early transition.

N-factors for a range of AoA are shown in Figures 22 and 23. Recall that wavelength is referenced as being parallel to the leading edge. There are several observations.

- Referring to both Figure 22, NLF (without DRE control) is likely up to 60% x/c on the suction side for AoA = 0° to 0.5°.
- Typically as one increases AoA, T-S destabilizes and crossflow stabilizes on the suction side because the pressure distribution steepens. The suction side has a T-S type breakdown due to the early suction peak at AoA ≈ +1°. In this instance the boundary-layer solution is unable to proceed downstream from the leading-edge due to the adverse region, and no LST results are shown because the flow has transitioned.

- Referring to Figure 22, DRE transition control of crossflow on the suction side appears feasible in the range of AoA between -0.5° and -1°. The favorable *Cp* region past about x/c = 10% has a steeper slope than that of the AoA = 0° case, which by comparison causes crossflow to be more unstable. Wavelengths in the range of 6 mm to 8 mm appear to be candidates for breakdown to transition. They appear to have the highest *N*-factors, high enough to likely cause transition, and are termed the "critical" wavelengths. These must be controlled if laminar flow is to be maintained. Further examining the LST results for these AoAs in Figure 22, it can be seen that crossflow of wavelengths on the order of 3 mm to 4 mm grow to *N*-factors of around 6 and then decay. These are candidate wavelengths for DRE control to stabilize the critical wavelengths and promote laminar flow. Li et al. (2010) independently studied the potential for DRE control at AoA = -1° based on the present airfoil shape, freestream conditions, and Euler solutions and using nonlinear parabolized stability equations and secondary instability theory to model the high-frequency instabilities known to cause breakdown. They found 2.67 mm and 4 mm wavelengths to be possible candidates for DRE control, though they noted some concerns about the control wavelengths themselves triggering transition at this particular AoA = -1°. These results are very encouraging for two reasons. First, we can increase the AOA to be larger than -1° (based on our own LST analysis) to lessen the initial growth of the control modes, if need be. As seen in Figure 22, we have flexibility to about AoA = -0.5°. Second, as mentioned above, this airfoil shape is not optimized because it hasn't yet been incorporated as the OML of the glove to be included in the iterations between full-aircraft CFD and stability analyses. From our previous experience and these preliminary results by Li et al. (2010), we are confident that we will be able to further refine the glove leading-edge C_p distribution (slightly steepen the initial slope) and generate the new OML to lessen the initial growth of the control modes, if need be, to meet DRE objectives.
- As mentioned above, demonstrating laminar flow on the pressure surface is a secondary objective of the flight experiment. Having said that and referring to Figure 23, the relatively flat favorable pressure gradient distribution means that crossflow should not be a concern, and NLF (without DRE control) is likely up to 40% *x/c* in a neighborhood of AoA = 0°. As one decreases AoA, T-S destabilizes and crossflow stabilizes because the pressure distribution steepens, and the pressure side appears to succumb to T-S type breakdown at angles of attack < 0 for this airfoil due to the adverse pressure gradient - in this instance the boundary-layer solution is unable to proceed downstream near the leading-edge due to the adverse region, and no LST results are shown. In the range of 0.5° to 1° AoA, critical crossflow wavelengths are on the order of 4 to 8 mm, and we believe that, once again, through further shaping the glove leading-edge C_p distribution (slightly steepening the initial slope) and generating the new OML, we can propose DRE control in the range of 2–3 mm.

To summarize, the combination of the following features make TAMU-003T-75 a candidate airfoil OML for further development into a wing glove: 1) the airfoil achieves a C_L as high as 0.49 2) the usable AoA range is reasonable, 3) the achieved thickness of 9.3% is ideal for mounting the wing glove on the G-II/SP, and 4) it is feasible to meet laminar flow objectives both through NLF techniques and through the application of DREs.

The next step would be to use this airfoil shape to design the wing glove and perform a full-aircraft Navier-Stokes flowfield computation including the engines, fairings, and streamline deflections. With this information, nonlinear parabolized stability equations (NPSE) calculations would be performed and the airfoil geometry and pressure distribution adjusted and iterated as necessary to achieve the desired stability behavior.

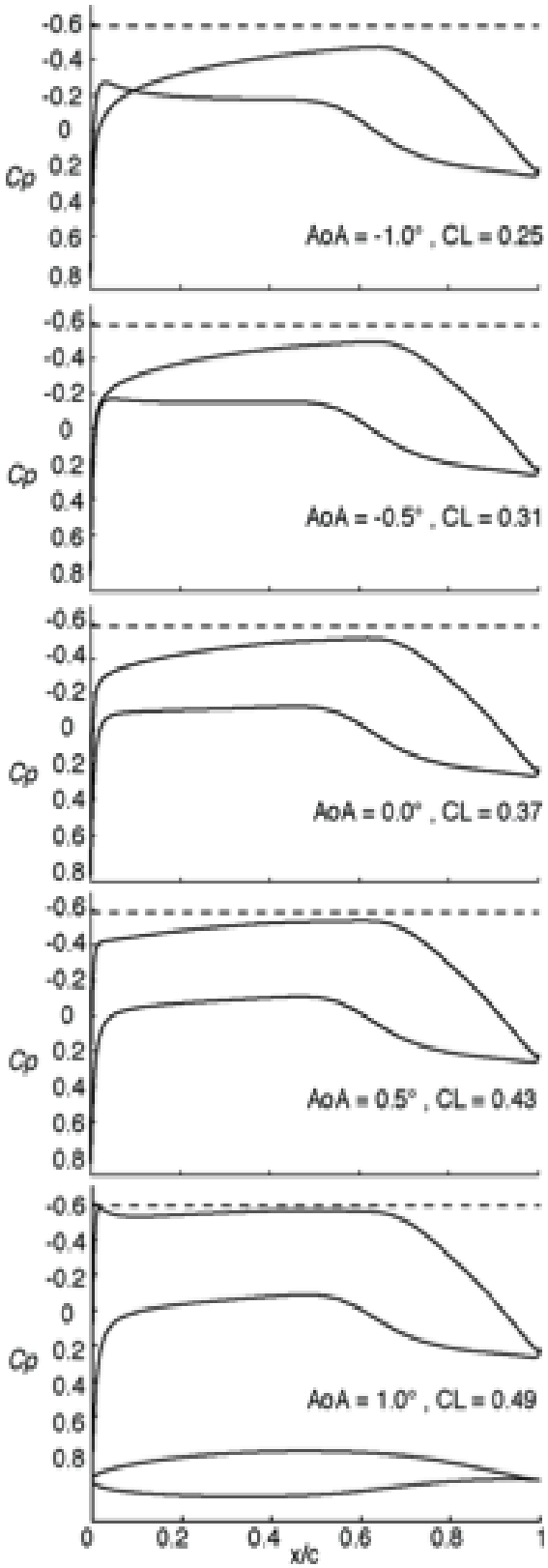

Figure 21. C_p for AoA in the range of +1° to -1°.

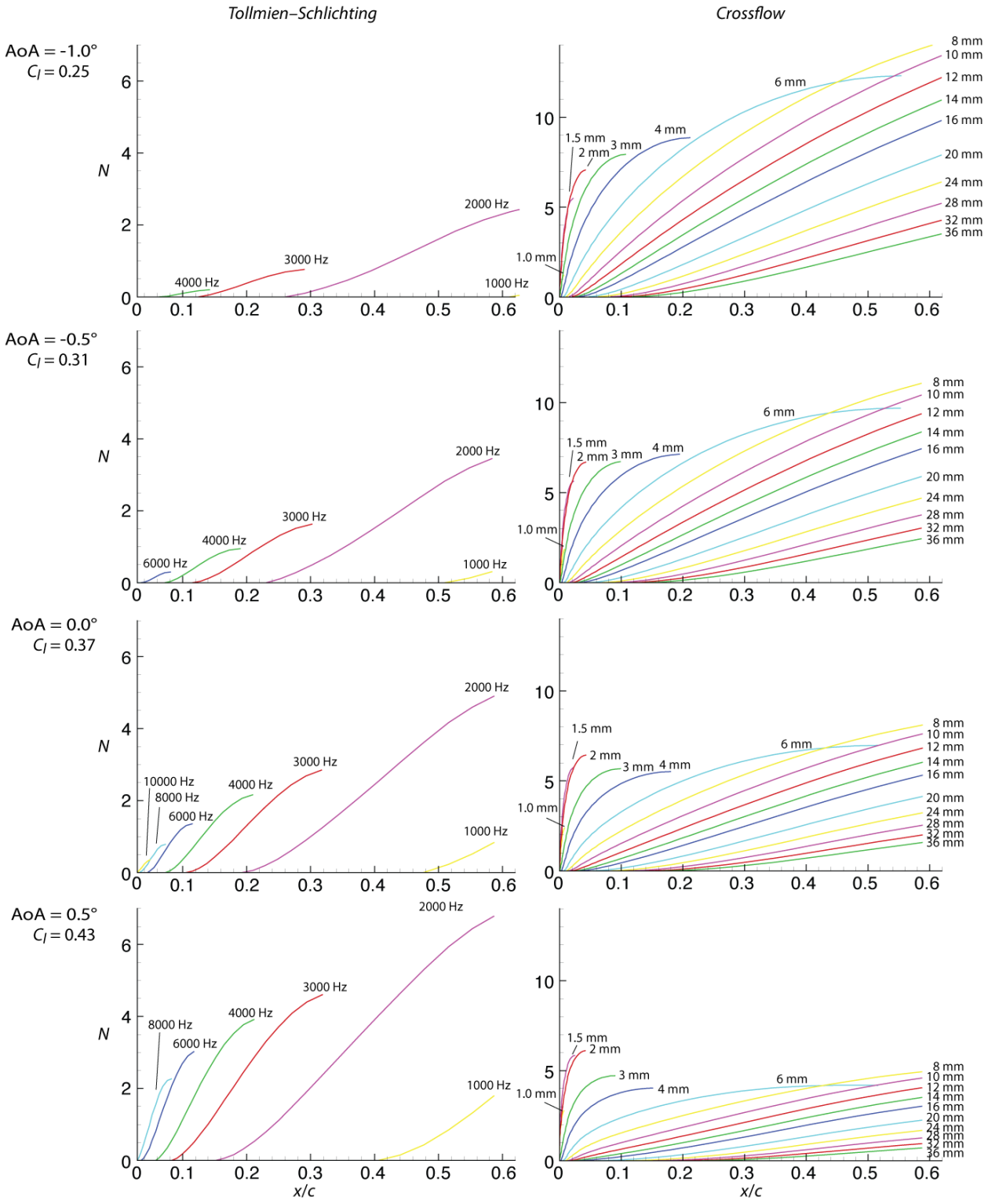

Figure 22. LST *N*-factor results over a range of angles of attack on the suction side of TAMU-003T-75. Here Re_c = 17.2M.

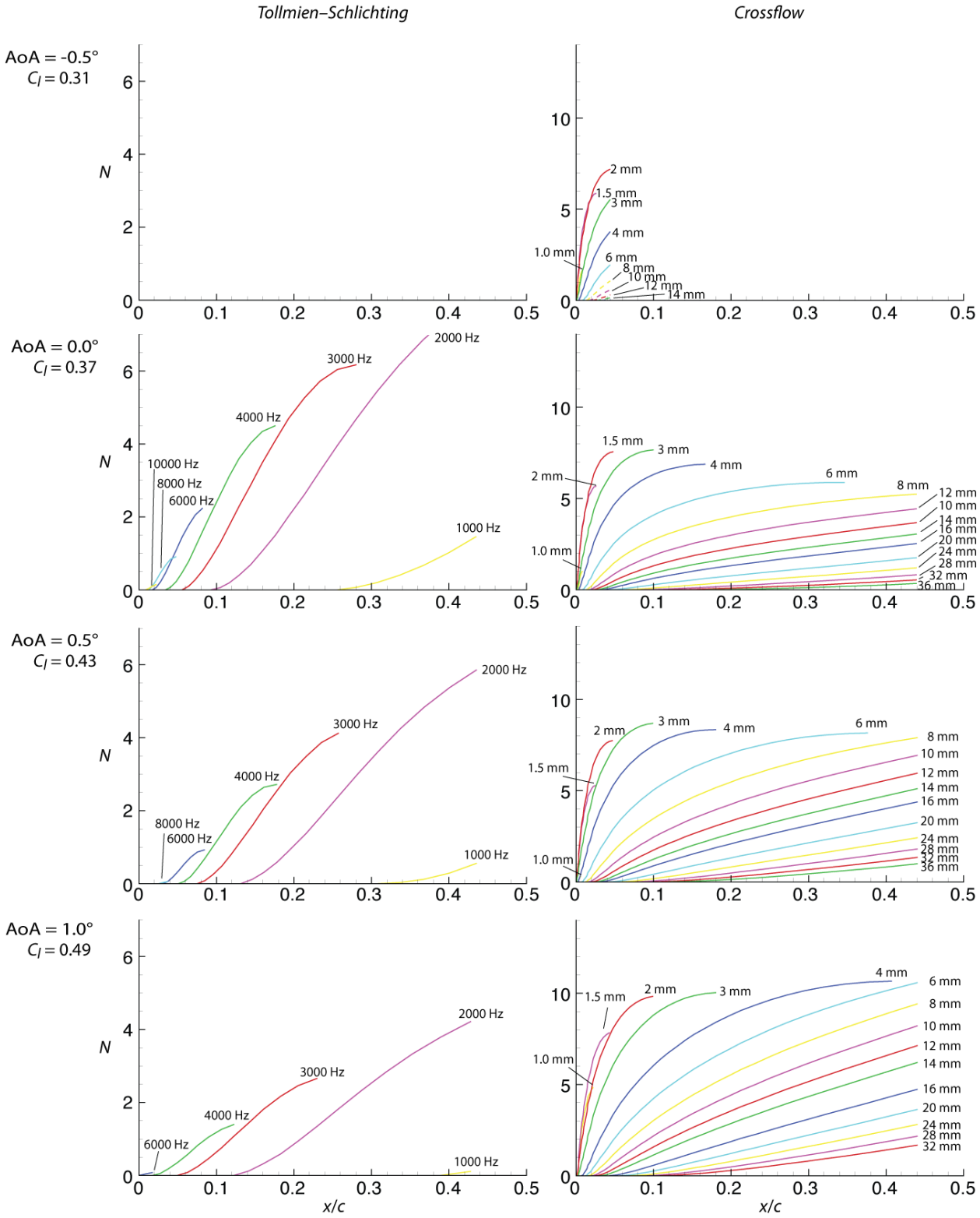

Figure 23. LST *N*-factor results over a range of angles of attack on the pressure side of TAMU-003T-75. Here Re_c = 17.2M.

V. Conclusions

To summarize, we believe we have answered the following key questions related to a flight experiment for extending DRE LFC efforts to higher chord Reynolds numbers between 15-20 million at unit Reynolds numbers on the order of 1.6 million per foot.

1) Is it possible to find an aircraft that can be used as a platform for this experiment?
   Yes, selection converged on the Gulfstream II (G-II) based on suitability and expected availability.

2) Given the aircraft, does a CFD of the aircraft flowfield show that there is no interference from engines that would compromise the experiment?
   Yes, a computational grid for the G-II was created, and engine nacelle effects are "accountable" in the outboard section and the flowfield is spanwise-uniform where the glove would be located. Moreover, streamline deflections are accountable including AoA and in-plane deflection effects on the glove.

3) Is it possible to design an airfoil with a representative C_l and C_p distribution that makes DREs feasible?
   Yes, airfoil section TAMU-003T-75 suggests that NLF is possible at AoA = 0°, with potential for DRE control between AoA = -0.5 and -1°.

A continuation of this experiment is in progress using the newly acquired NASA DFRC Subsonic Research Aircraft (SCRAT) Gulfstream III (G-III). This experiment is the first flight-test experiment that will be performed as a part of the NASA Environmentally Responsible Aircraft project (Collier, 2010). The G-III is a more desirable aircraft for this experiment. Additionally, since many features of the G-II and G-III are similar, the lessons learned in this study are directly applicable to the new aircraft platform. Detailed airfoil design has started again for G-III conditions, with the intent to introduce DRE control at Re_c between 22-30 million. Full-aircraft CFD studies (including the engines) are once again underway to determine wing glove placement on the G-III. Once a candidate airfoil is determined for a possible OML, the wing glove and fairings will be modeled in a full-aircraft Navier-Stokes simulation coupled with NPSE calculations, and the airfoil geometry and pressure distribution adjusted and iterated as necessary to achieve the desired stability behavior. The NPSE work will provide the proper assessment of the efficacy of the DREs in suppressing the growth of the most unstable stationary crossflow wave. Flight tests are expected to begin in 2011.

Acknowledgments

This work was supported under AFOSR/NASA grant FA955008-1-0475.

The present work is part of a collaborative effort with NASA Langley Research Center and NASA Dryden Flight Research Center. Technical interactions with the NASA Centers are gratefully acknowledged.

The contributions of Texas A&M University graduate students Matthew Roberts, Matthew Woodruff, and Matthew Tufts are greatly appreciated.

References

"Advances in laminar-turbulent transition modelling," *AVT-151 RTO AVT/VKI Lecture Series*, North Atlantic Treaty Organization, Rhode St. Genese, Belgium, 2009.

Boppe CW. 1984. Elements of computational engine-airframe integration. *AIAA-1984-0117*.

Carpenter A, Saric W, Reed H. 2010. Roughness receptivity in swept-wing boundary layers – experiments. *International Journal of Engineering Systems Modeling and Simulation,* Vol. 2, No. 1/2, 128-138, March 2010.

Chang C. 2003. The Langley stability and transition analysis code (LASTRAC): LST, linear & nonlinear PSE for 2-D, axisymmetric, and infinite swept wing boundary layers. *AIAA-2003-0974.*

Chang C, Choudhari M. 2005. Boundary-layer receptivity and integrated transition prediction. *AIAA-2005-0526.*

Collier, F. 2010. Overview of NASA's Environmentally Responsible Aviation (ERA) project: A NASA Aeronautics project focused on midterm environmental goals. Presented at the *28th AIAA Applied Aerodynamics Conference*.

Drela M, Youngren H. 2001. *XFOIL 6.9.* http://web.mit.edu/drela/Public/web/xfoil/.

Flack R. 2005. *Fundamentals of jet propulsion with applications.* Cambridge University Press, New York, pp 212-213.

FLUENT, Software Package, Ver. 12.0.16, ANSYS Inc., Canonsburg, PA, 2010.

Jane's Aircraft Upgrades [online database], 2009, http://jau.janes.com/.

GAMBIT, Software Package, Ver. 2.3.16, ANSYS Inc., Canonsburg, PA, 2010.

Li F, Choudhari M, Carpenter M, Malik M, Chang C, Street C. 2010. Roughness based crossflow transition control for a swept airfoil design relevant to subsonic transports. *AIAA-2010-4380*

Mattingly J, von Ohain H. 2006. *Elements of propulsion: gas turbines and rockets*. AIAA Education Series, AIAA.

Mund F, Doulgeris G, Pilidis P. 2007. Enhanced gas turbine performance simulation using CFD modules in a 2D representation of the low-pressure system for a high-bypass turbofan. *Journal of Engineering for Gas Turbines and Power*, Vol. 129, July, pp. 761-768.

Pfenninger W. 1965. Some results from the X-21 program. Part I. Flow phenomenon at the leading edge of swept wings. *AGARDograph No. 97*.

Pfenninger, W. 1977. Laminar flow control – laminarization. *Special Course on Drag Reduction, AGARD Report 654*, Von Kármán Institute, Rhode-St. Genese, Belgium.

Pruett C. 1994. A spectrally accurate boundary-layer code for infinite swept wings. *NASA Contractor Report 195014*.

Rhodes R, Reed H, Saric W, Carpenter A., Neale T. 2010. Roughness receptivity in swept-wing boundary layers – computations. *International Journal of Engineering Systems Modeling and Simulation*, Vol. 2, No. 1/2, 139-148, March 2010.

Rizzetta D, Visbal M, Reed H, Saric W. 2010. Direct numerical simulation of discrete roughness on a swept wing leading edge. *AIAA-2010-377*, submitted to *AIAA Journal*.

Saric W, Carrillo R, Reibert M. 1998. Leading-edge roughness as a transition control mechanism. *AIAA Paper No. 98-0781*.

Saric W, Reed H, Banks D. 2004. Flight testing of laminar flow control in high-speed boundary layers. *NATO-RTO-MP-AVT-111*, Prague, Oct.

Saric W, Carpenter A, Reed H. 2010. Passive control of transition with roughness in three-dimensional boundary layers. *Philosophical Transactions of the Royal Society A* (2010), to appear.

Seddon J, Goldsmith E. 1999. *Intake aerodynamics*, 2nd ed., AIAA Education Series, AIAA.